Parametric Analysis of the Spatial Resolution and Signal-to-Noise Ratio in Super-Resolved Spatiotemporally Encoded (SPEN) MRI

Noam Ben-Eliezer,[1]* Yoav Shrot,[2] Lucio Frydman,[2] and Daniel K. Sodickson[1]

Purpose: Spatiotemporally Encoded (**SPEN**) MRI is based on progressive point-by-point refocusing of the image in the spatial rather than the k-space domain through the use of frequency-swept radiofrequency pulses and quadratic phase profiles. This technique provides high robustness against frequency-offsets including B_0 inhomogeneities and chemical-shift (e.g., fat/water) distortions, and can consequently perform fMRI at challenging regions such as the orbitofrontal cortex and the olfactory bulb, as well as to improve imaging near metallic implants. This work aims to establish a comprehensive framework for the implementation and super-resolved reconstruction of SPEN-based imaging, and to accurately quantify this method's spatial-resolution and signal-to-noise ratio (SNR).

Theory and Methods: A stepwise formalism was laid-out for calculating the optimal experimental parameters for SPEN, followed by analytical analysis of the ensuing SNR and spatial-resolution versus conventional k-space encoding. Predictions were then confirmed using computer simulations and experimentally.

Results: Our findings show that SPEN is governed by the same fundamental signal-processing principles as k-space encoding, leading to similar averaging properties, and ultimately similar spatial-resolution and SNR levels as k-space encoding.

Conclusion: Presented analysis is applicable to general multi-dimensional SPEN designs and provides a unified framework for the analysis of future SPEN and similar approaches based on quadratic phase encoding. **Magn Reson Med 72:418–429, 2014. © 2013 Wiley Periodicals, Inc.**

Key words: spatiotemporal encoding; super-resolution; Frequency-swept pulses; non-Fourier methods; signal-to-noise ratio

INTRODUCTION

The use of magnetic field gradients constitutes one of the cornerstones of spatial encoding in MR imaging. Practically unchanged at a fundamental level since its first implementation (1), this scheme uses linear field gradients for encoding the spatial domain, followed by Fourier Transformation (**FT**) of the ensuing signal to recover the desired image. Recently, an alternative encoding technique, termed spatiotemporal-encoding (**SPEN**), has emerged, which uses quadratic rather than linear phase profiles to extract the spatial information (2). The quadratic phase profile focuses the signal to arrive from a region around its vertex where all the spins are in-phase, while largely suppressing signals from other regions where spins destructively interfere with each other. Imprinting such phase profiles can be accomplished in several different ways, arguably the simplest of which, relies on the use of frequency swept radiofrequency (**RF**) pulses. This reliance on such pulses in the context of MR imaging is indeed not unique and has been reported in the past, e.g., by Kunz and Hilal for reducing peak RF power (3,4); by Maudsley for decreasing the dynamic range of the acquired signal (5); and by Pipe for improved slice-encoding, enhanced slice definition, and the prevention of aliasing when using limited fields of view (FOVs) (6). More recent implementations of quadratic phases for MRI include PatLoc and O-space imaging (7–9); these should be distinguished from SPEN as they involve customized nonlinear gradient hardware, and use different reconstruction procedures than the one to be discussed herein.

Selected examples of SPEN's performance vis-à-vis conventional k-space encoding are illustrated in Figure 1. In its simplest form, SPEN relies on exciting the sample's spins using a frequency swept RF pulse applied in tandem with a magnetic field gradient G_{exc}, which acts to spread out the resonance frequencies throughout the axis to be encoded. The RF pulse progressively sweep over this range of frequencies, thereby exciting different locations at different times. The postexcitation quadratic phase profile is then equal to (2),

$$\phi_{exc}(x) = \frac{\gamma^2 G_{exc}^2}{2R} x^2 - \frac{\gamma^2 G_{exc}^2 FOV}{2R} x \qquad [1]$$

where T_{exc} is the RF duration, FOV is the imaged field-of-view, $R \equiv \gamma G_{exc} FOV / T_{exc}$ is the RF sweep rate (in units of frequency / time), and γ is the gyromagnetic ratio. The quadratic shape of ϕ_{exc} causes the spins' phase to vary rapidly across the sample except around a stationary phase region, whose characteristic width is equal to (10),

$$\Delta x = \frac{\sqrt{R}}{\gamma G_{exc}} \qquad [2]$$

Relying on these principles, the spin density profile $\rho(x)$ can subsequently be read out using an acquisition gradient G_{acq}. This adds a linear phase term $\phi_{acq} =$

[1]The Bernard and Irene Schwartz Center for Biomedical Imaging, Department of Radiology, New York, University School of Medicine, New York, New York, USA.

[2]Department of Chemical Physics, Weizmann Institute of Science, Rehovot, Israel.

*Correspondence to: Noam Ben-Eliezer, Ph.D., The Bernard and Irene Schwartz Center for Biomedical Imaging, Department of Radiology, New York, University School of Medicine, New York, NY.
E-mail: noam.ben-eliezer@nyumc.org

Additional Supporting Information may be found in the online version of this article.

Received 28 March 2013; revised 18 August 2013; accepted 21 August 2013

DOI 10.1002/mrm.24954
Published online 17 October 2013 in Wiley Online Library (wileyonlinelibrary.com).

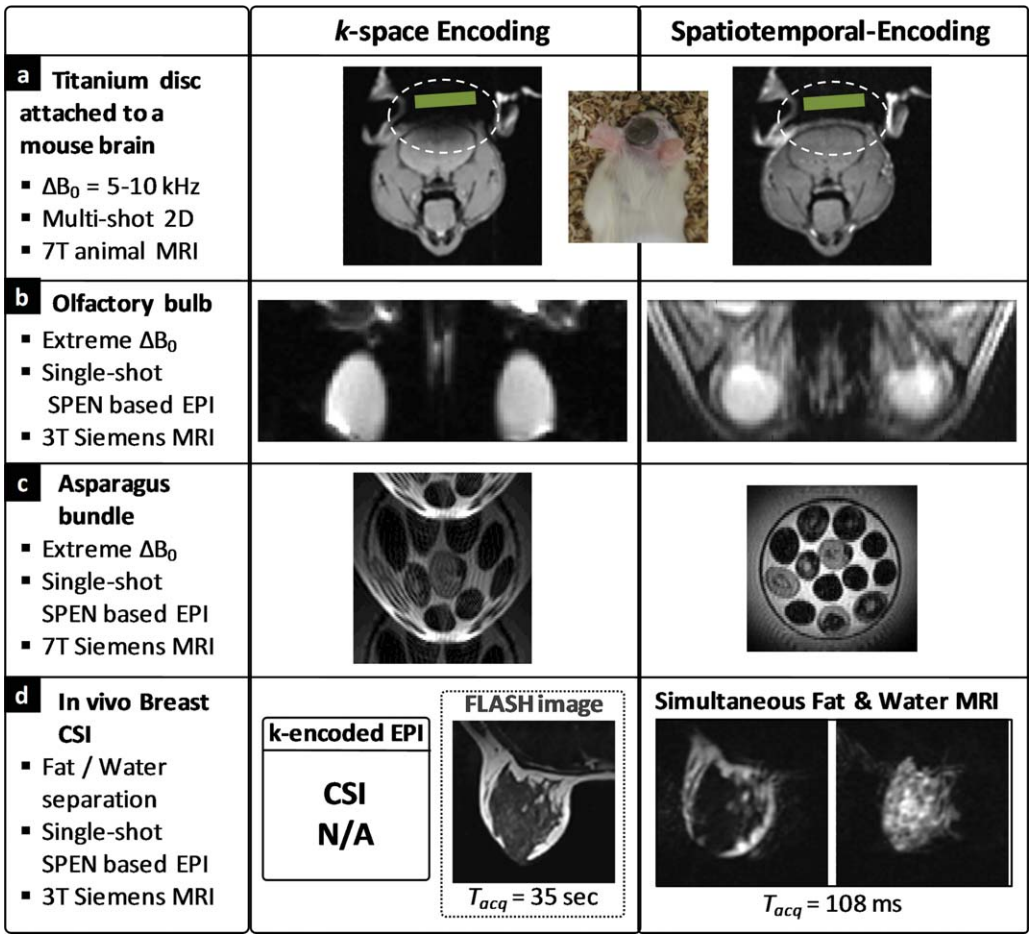

FIG. 1. Examples of spatiotemporally encoded MRI versus conventional k-space encoded imaging. **a:** Multi-shot spin-echo images of a mouse brain demonstrating the ability of SPEN to overcome extreme field inhomogeneities induced by a titanium disc at 7T [Varian microimaging vertical scanner; disc diameter = 18 mm, thickness = 3 mm] (15). b–d: Single-shot spin-echo EPI (SE-EPI) versus SPEN based EPI images exemplifying SPEN's ability to: **b:** overcome strong susceptibility distortions occurring near the olfactory bulb of a human volunteer [Siemens whole body 3T scanner, slice-thickness = 5mm, pixel-size = 1.875 × 1.875 mm^2, (for SE-EPI) and 1.5 × 1.5 mm^2 (for SPEN)]. SPEN's main advantage originates, in this case, from its ability to perform partial FOV imaging, while using higher bandwidth per pixel along the PE direction (39.0 versus 11.3 Hz/Px) without being penalized by folding artifacts (11,21); **c:** overcome the strong B_0 field inhomogeneities, occurring at 7T high-field systems through the self-refocusing feature allowing more effective spin-echo refocusing [Siemens whole-body scanner, pixel-size = 1.0 × 1.0 mm^2, TE = 149 ms for SE-EPI and 156 ms for SPEN, slice-thickness = 2 mm, bandwidth per pixel along the PE direction = 11 Hz/Px for SE-EPI and 12 Hz/Px for SPEN); **d:** simultaneously encode and reconstruct images of multiple chemical-sites (in this case of fat and water), as compared to conventional EPI where single-shot CSI led to incoherently overlapped images of fat and water that cannot be separated in post-processing (Siemens whole-body 3T scanner) (19).

$\gamma G_{acq} tx \equiv k(t)x$, causing the stationary point to traverse the encoded x-axis while its intensity reflects the spin density at each region. Assuming sufficient spatial localization is achieved during the encoding process, i.e., that the phase profile in Eq. [1] is sharp enough, a straightforward signal-magnitude operation can then produce an image profile by means of $\rho(x) \propto |S(t)$, without the use of Fourier Transformation. As shown in detail in (11,12) the spatially sequential excitation and acquisition processes also allow SPEN, under the condition $T_{exc} = T_{acq}$, to implement a unique type of spin-echo (**SE**) in which the excitation-τ-refocusing-τ-acquisition condition is met for each and every signal point and not just for the center signal point as in classic k-space encoding. Adding to that the fact that in SPEN each spatial region is sampled during a period shorter than the total acquisition time, T_2* effects have less time to evolve, giving rise to the improved immunity to off-resonance artifacts reported in (12–17) and exemplified in Figure 1. Further features of SPEN include its ability to encode multiple chemical sites during a standard imaging scan, allowing straightforward implementation of chemical-shift-imaging (CSI) (18) (Fig. 1d) and providing robust protection against fat/water artifacts (19); and the lack of Nyquist ghosting artifacts as a consequence of SPEN's circumvention of a FT (Fig. 1b,c). The latter property is indeed an outcome of processing SPEN data using techniques that are tailored to its unique spatiotemporal nature. Such techniques will, in the context of single-shot imaging, provide SPEN-based protocols with two additional advantages. The first, relates to SPEN's capability to acquire partial FOVs for a fixed matrix size without suffering from folding artifacts. Examples of image reconstruction approaches that very efficiently use this property are given in (20,21). The second

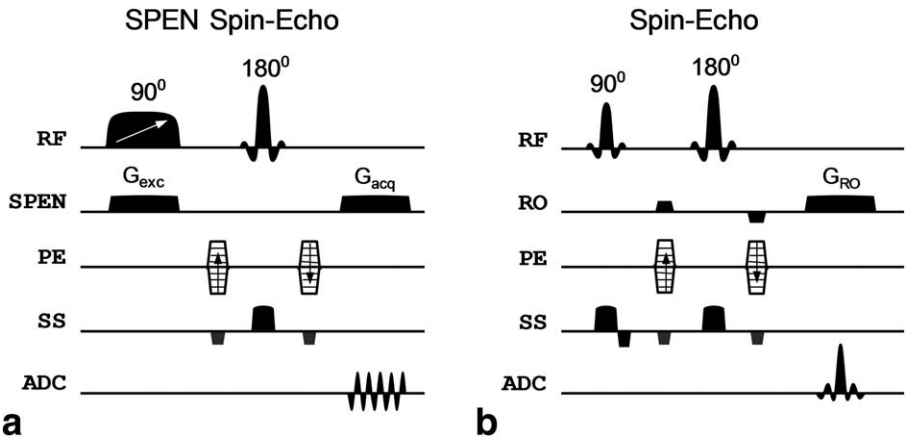

FIG. 2. Pulse sequence scheme for a multi-slice spin-echo protocol based on (**a**) spatiotemporal-encoding and (**b**) conventional k-space encoding. Implementation of SPEN along the readout (RO) dimension involves replacing the slice-selective excitation with a frequency swept RF pulse, acting in unison with a field gradient G_{exc}, to generate a quadratic phase profile along the SPEN axis. The focal point created by this phase profile is then traversed during the acquisition, along the encoded axis using a G_{acq} gradient, to produce a signal that is composed of a continuous series of spatially localized spin-echoes. Identical encoding is used along the remaining dimensions in both (a) and (b), using phase-encoding (PE) and slice-selection (SS). Image reconstruction follows the super-resolution algorithm for the SPEN axis (26), and Fourier Transformation for the k-space encoded axis, as well as for the PE dimension in both sequences.

advantage consists of the ability to use of higher bandwidths along the phase-encoded (PE) dimension in EPI scans, thereby significantly reducing B_0 inhomogeneity and motion artifacts that typically affect this dimension in single-shot imaging (11,12).

SPEN constitutes a generic encoding scheme which can be incorporated into arbitrary imaging protocols. Figure 2 illustrates a spin-echo implementation (SE SPEN), in which k-space encoding along the readout channel is substituted by SPEN. The diagram also highlights a potential drawback of SPEN; namely, that the use of a nonselective frequency swept excitation pulse calls for the use of a slice-selective refocusing pulse for restoring the protocol's slice-selectivity. This being said, SPEN spin-echo protocols such as the one shown in Figure 2 still lack straightforward slice-interleaving capabilities, requiring the use of customized implementations when using SPEN for volumetric acquisitions (16,22). Another potential limitation of SPEN's quadratic phase encoding rests in the loss in signal-to-noise ratio (**SNR**), which could arise from the high spatial locality required to achieve similar spatial resolutions as in k-space encoding (23,24). At this extreme limit, a simple magnitude operation $\rho(x) \propto |S(t)|$ could lead to SNR losses of up to $\sqrt{N}$, the square root of the number of acquisition points (25). In a recent report, we introduced a conceptually different approach to the implementation of SPEN MRI, which addresses this penalty using a signal reconstruction procedure based on super-resolution (**SR**) principles (26). In this case, a several-pixel-wide focal point can be encoded using SPEN's usual scheme, while the ensuing image resolution is restored using an SR-based algorithm that makes use of multiple signal points for the calculation of each image point. In this manner, SPEN can depart from the one-pixel-wide focal point limit and reintroduce the multiplexing advantage into SPEN, resulting in a substantial enhancement of the final SNR. In this report we investigate the theoretical aspects of SR SPEN, centering on the analysis of its spatial resolution and SNR in comparison to conventional k-space encoded MRI. To do so we start by laying out a stepwise parametric framework for the implementation of SR SPEN imaging at the parametric limit defined by k-space encoding, and follow with a theoretical derivation of the corresponding signal-to-noise ratio. As will be discussed later, this choice, although allowing objective comparison of the two encoding techniques, is not restrictive, as SPEN can still depart from the spatially global limit defined by the k-space formalism, trading off SNR and/or specific absorption rate (SAR) for higher spatial localization. Validations of both SNR and spatial resolution properties are presented using computer simulations and experiments.

THEORY

Parametric Framework of Super-Resolved SPEN MRI

A detailed description of SPEN's super-resolution reconstruction algorithm can be found in Ben-Eliezer et al (26). We restrict ourselves here to the reiteration of some key features of this encoding scheme, and continue by presenting a new framework that can serve as a general basis for implementing SR SPEN protocols with optimal resolution and sensitivity. During a SPEN experiment, magnetization is modulated by a combination of the (quadratic) excitation phase, and a linear acquisition phase. The acquired signal can be expressed as

$$S(t_n) = \int \exp\left[-i\phi_{exc}(x) + ik(t_n)x\right]\rho(x)dx = \mathbf{E}\rho \qquad \text{n} = 1, 2, \ldots, N \qquad [3]$$

where the sign of ϕ_{exc} was flipped to account for a spin-echo refocusing pulse acting before the signal acquisition, and **E** is an operator representing the set of spatially continuous modulations imposed by the acquisition procedure and associated with digitized measurements at times t_n. The resulting pixel size then becomes either

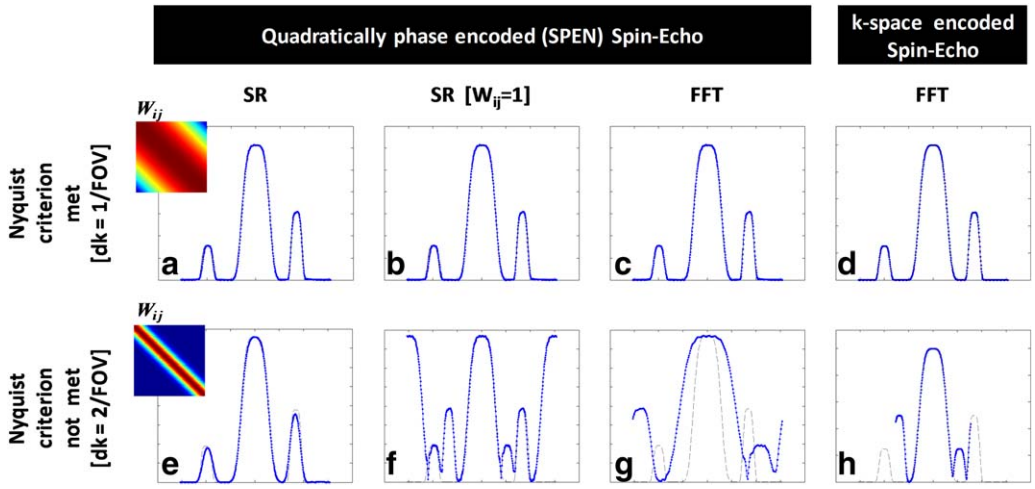

FIG. 3. Simulated spin-echo images comparing quadratic phase encoding (SPEN) versus linear (k-space) encoding, at, and below the sampling conditions defined by Nyquist-Shannon criterion. For all panels, the original image profile is denoted by a gray dashed line. SPEN images were produced using full SR reconstruction (**a,e**); modified SR reconstruction using constant spatial weights $W_{u,n}=1$ (**b,f**); or using direct Fourier Transform (FT) (**c,g**). k-space encoded images were reconstructed using FT (**d,h**). Top row: when matching the sampling rate to the Nyquist criterion, SPEN and k-space encoding provide similar images using any of the reconstruction variants. Bottom row: reducing the sampling rate below the Nyquist criteria leads to image aliasing (folding artifacts). These are expressed either as (f): repeated replication of the image along the full FOV, or (g,h): aliased images, which in the case of FT reconstruction, span only half the original FOV. Using spatially localized weighting $W_{u,n}$ in the SR reconstruction allows restoration of the original image profile, at a tradeoff of $\times 2$ lower spatial resolution (e). Simulations used identical imaging parameters for SPEN and k-space encoding (e.g., sequence timing, spatial resolution, FOV, acquisition bandwidth, spin-echo pulse etc.), excluding the encoding RF which used a 3-ms frequency swept pulse for SPEN versus a 3-ms two-lobe SINC pulse for k-space encoded images. [Color figure can be viewed in the online issue, which is available at wileyonlinelibrary.com.]

equal to, or larger than the optimal value $dx = FOV/N$, by a super-resolution factor F_{SR} defined as

$$F_{SR} = \Delta x/dx(\geq 1) \quad [4]$$

F_{SR} reflects the spatial resolution penalty, paid upon processing SPEN images using magnitude-mode reconstruction. Its ≥ 1 nature, however, suggests the possibility of restoring the missing information using a more advanced postprocessing procedure. The SR reconstruction does exactly that by using an estimated inverse of the encoding matrix **E**. Because a pure mathematical inverse does not necessarily exist for **E**, this reconstruction cannot follow a simple model-inversion procedure. Instead, SR relies on a least square minimization (LSM) of the cost function

$$\arg\min_{\rho} \| \rho(x) - \mathbf{P}(x,t)S(t) \|_2 \quad [5]$$

where $\rho(x)$ denotes the unknown target profile having a full spatial resolution of N pixels, and **P** represents a customized discrete reconstruction model, approximating the inverse of **E**. Suitable choices of discretization may be made in analogy to the case of weak and strong SENSE (27), or other generalized parallel image reconstructions (28). As was reported in (26), a judicious choice for **P** will be given by the Hermitian conjugate of the acquisition operator sampled at the desired voxel center positions, and weighted by an appropriate intra-voxel average. Although this choice might not be the most accurate pseudoinverse of **E**, it was found to be optimal both in terms of its ensuing SNR and of the final image resolution. This choice for the reconstruction matrix can be written as

$$\mathbf{P}_{u,n} = W_{u,n}\exp\left[-(-i\phi_{exc}(x_u) + ik(t_n)x_u)\right]u, n = 1,2,\ldots,N \quad [6]$$

The weighting matrix W introduced in this equation represents the intra-voxel dephasing caused by the strong phase variations along the sample. Similar to the stationary-phase condition taking place during SPEN acquisition, **P**'s quadratic phase reflects a time- and space-dependence that acts to vary the relative contribution of each signal point by inducing strong dephasing at all regions, except at its vertex. The real-valued weighting matrix W accounts for this feature at a sub-voxel level by interpolating the spatial dimension of the discrete phase matrix by a certain factor M, and then averaging over the M complex exponents that comprise each voxel to retrieve its net contribution:

$$W_{u,n} = \left|\sum_{j=1}^{M}\exp\left[-\left(-i\phi_{exc}(x_j) + ik(t_n)x_j\right)\right]\right| x_j \in [x_u \ldots x_{u+1}] \quad [7]$$

This procedure corresponds approximately to a fit of the continuous SPEN phase modulation functions to rectangular voxels of the desired width. Numerically, we found that interpolation factors of $M = (10\ldots20)$ are sufficient to account for the subvoxel dephasing effects, while values above 20 had no effect on the ensuing weighting matrix. An instructive example of the role played by the weighting matrix W is given in Figure 3, demonstrating SPEN's ability sample a signal at a sub-Nyquist level, while trading off some of the image's spatial resolution. This feature can, for example, be used when employing SPEN along the PE dimension of single

shot pulse sequences. In such cases, it is possible to increase the bandwidth along the PE dimension, without being affected by folding artifacts as a result of using larger dk_{PE} values (whereas the same step would result, for the case of k-space encoding, in truncation of the image and folding artifacts). As mentioned before, the same feature is also advantageous in cases where the region of interest does not cover the entire FOV, by enabling one to scan limited FOVs without being affected by aliasing artifacts and with no loss of spatial resolution (11,20,21). As a final step, we use the reconstruction model in Eq. [6] to express SPEN's super-resolved PSF in an analytical form: by sequentially applying the encoding and reconstruction operators one obtains

$$PSF_{SPEN} = \mathbf{PE} \qquad [8]$$

The robustness of the resulting SR reconstruction procedure for restoring optimal image resolution has been demonstrated for a variety of SPEN pulse-sequence schemes, and in the context of both single- and multi-shot imaging (15,22,29,30). The optimal resolution enhancement will, by definition, be limited to F_{SR} seeing as the number of final image pixels cannot, in the absence of prior information, exceed the number of acquired signal points. To formulate a clear relationship between the experimental parameters and the reconstructed image properties, we examine in further detail SPEN's signal acquisition process. The key point to remember is that, in common with most digital sampling processes, the minimum frequency difference that SR SPEN-based protocols will be able to discern, is given by the reciprocal of the overall acquisition duration, namely: $d\upsilon = 1/T_{acq}$. Considering that in MR imaging the frequency axis corresponds to a magnetic field gradient ($\upsilon = \gamma Gx$), this condition can be cast into the spatial domain, yielding a maximal spatial resolution of

$$dx = \left(\gamma G_{acq} T_{acq}\right)^{-1} \equiv k_{\max}^{-1} \qquad [9]$$

where we have used the classical k-space notation to denote the reciprocal of the acquisition gradient first moment. Given a target field-of-view *FOV* and spatial-resolution *dx*, Eq. [9] can be used to determine SPEN's acquisition bandwidth, which becomes $BW_{acq} = \gamma G_{acq} FOV$. Finally, we note that in order for SPEN's quadratic-phase focal point to sweep over the entire FOV during the acquisition process, the excitation and acquisition parameters need to match one another, thereby creating a parametric link between these two stages according to $\gamma G_{exc} T_{exc} = \gamma G_{acq} T_{acq}$ (12). This link will in turn define the encoding RF time-bandwidth product (**TBP**) and can be summarized as,

$$RF_{TBP} = T_{exc} \cdot \gamma G_{exc} FOV = \gamma G_{acq} T_{acq} FOV \qquad [10]$$

Equation [10] constitutes one of the key relations in SPEN imaging by establishing a parametric link between the acquisition and excitation events wherein the excitation RF parameters are derived from the target image resolution and FOV. The same RF time-bandwidth product can, furthermore, be related to the non–super-resolved pixel size by means of $\Delta x = FOV/\sqrt{RF_{TBP}}$ (see Tal and Frydman) (10) and hence, sets a fixed value for the SR enhancement factor in Eq. [4]. We thus conclude that by setting a target FOV, spatial-resolution, and acquisition bandwidth, a deterministic stepwise set of relations dictates both the experimental parameters and the optimal reconstruction enhancement achievable by SR-SPEN.

Signal-to-Noise Ratio in SR SPEN MRI

The introduction of SR reconstruction into SPEN constitutes a shift from a strictly localized acquisition regime, toward a pseudo-local one. Besides enhancing SPEN's spatial definition by a factor $F_{SR} = \Delta x/dx$, this procedure also manifests a dual multiplexing advantage – initially during the actual acquisition process, when instead of localizing the signal to a single pixel-wide region *dx*, the focal point is broadened to span a range of $dx \cdot F_{SR}$ pixels; and subsequently, during reconstruction when a consecutive set of F_{SR} signal points are multiplexed for the calculation of each image point. Factoring in the fact that an image's intensity is proportional to its underlying pixel size, this twofold advantage can be formulated to describe the intensity of a SR SPEN image by,

$$\hat{S}^{SPEN} \sim dx \cdot F_{SR}^2 \qquad [11]$$

It can be further shown (see Appendix A) that by requiring SR reconstruction to restore an optimal image resolution of *N* pixels, this SR enhancement factor will obey $F_{SR} = \sqrt{N}$, reducing Eq. [11] to,

$$\hat{S}^{SPEN} \sim dx \cdot N \qquad [12]$$

This signal should be compared with the levels in an analogous FT imaging experiment, based on k-space encoding. In this case, the FT postprocessing operation multiplexes the entire set of *N* acquired points for the calculation of each image pixel, leading to a corresponding *N* fold enhancement of the signal. The resulting image intensity thus assumes a similar value as the one obtained by SPEN:

$$\hat{S}^{k-enc} \sim dx \cdot N \qquad [13]$$

Focusing next on a noise level analysis, we examine a SPEN time-domain signal noise, represented by a characteristic standard-deviation (**STD**) of each acquired signal points. This value is in turn proportional, through the noise correlation matrix Ψ, to the digital filter bandwidth used to sample the analog signal. Without loss of generality we will restrict this analysis to a single coil setup, reducing Ψ to a scalar σ. Denoting the discretized time-domain noise by a vector η_k taken to have zero-mean Gaussian distribution, its STD can be expressed by,

$$\chi^{(k)} = \left[\overline{\langle \eta_k | \eta_k \rangle}\right]^{1/2} = \left[\sigma BW_{acq}\right]^{1/2} \qquad [14]$$

where the bra-ket notation denotes a complex transpose multiplication, and the overhead bar indicates an ensemble average over a set of independently acquired noise vectors. To assess the final image noise we transform the time-domain noise vector to the image-domain using the same reconstruction model in Eq. [6]. This yields,

$$\eta_x = \mathbf{P}\eta_k \quad [15]$$

SR SPEN's image noise STD $\chi^{(x)}$ can be now calculated in a similar manner:

$$\chi^{(x)}_{SPEN,i} = \left[\overline{\langle \mathbf{P}\eta_k|\mathbf{P}\eta_k\rangle}_{ii}\right]^{1/2} = \left[\overline{\langle \eta_k|\mathbf{P}^\dagger\mathbf{P}|\eta_k\rangle}_{ii}\right]^{1/2} = \chi^{(k)}\sqrt{\sum_p \mathbf{P}^*_{p,i}\mathbf{P}_{i,p}} \quad i = 1,2,\ldots,N \quad [16]$$

where N is the number of image pixels. Similar to Eq. [14], the last expression represents an ensemble average over a set of independently reconstructed noise vectors, and has a matrix form whose diagonal elements $\langle\rangle_{ii}$ denote the noise STD of each image pixel—i.e., the quantity being sought—and whose off-diagonal elements represent inter-pixel noise correlations, a quantity not relevant to the analysis at hand. Notice that the SR-derived enhancement of the noise STD embodied in the rightmost term of Eq. [16], depends solely on the reconstruction model **P**. As this is analytically known (Eq. [6]), it can be used to directly calculate the value of $\chi^{(x)}_{SPEN}$ at each pixel. Seeing as the last steps do not make any assumptions concerning the type of reconstruction model used, a very similar noise-analysis procedure can be followed to evaluate the effects of applying a FT to conventionally acquired k-space data. Using identical acquisition bandwidths, the time-domain noise STD will be identical to the one given in Eq. [14]. Taking the inverse of the encoding operator $IFT = \exp(-ikx)$ as the reconstruction operator, the image domain noise STD then becomes,

$$\chi^{(x)}_{FT,i} = \left[\overline{\langle \eta_k|FT^\dagger FT|\eta_k\rangle}_{ii}\right]^{1/2} = \sqrt{N}\chi^{(k)} \quad \forall i \in [1\ldots N] \quad [17]$$

The last simplifying step uses the fact that FT matrices have constant eigenvalue magnitudes, all equal to $\sqrt{N}$ (31). Combining Eqs. [12] and [16] for SPEN, and [13] and [16] for k-space encoding, we can now formulate a theoretical estimate for the relative SNR of SPEN versus k-space encoding,

$$\left.\frac{SNR^{SPEN}}{SNR^{k-enc}}\right|_{theory} = \sqrt{\frac{N}{\sum_p \mathbf{P}^*_{p,i}\mathbf{P}_{i,p}}} \quad [18]$$

This relation is indeed valid for any single-coil SPEN reconstruction model and for any set of parameters, and will be used to analyze the simulated and experimental data SNR.

METHODS

Computer Simulations of SR SPEN's PSF and SNR Values

Computer simulations were performed for estimating SR SPEN's point-spread-function and signal-to-noise ratio, as well as for comparing against k-space encoded MRI. The simulations provided an optimal framework for comparing the two encoding methods, free of various scanner- and object-dependent factors such as B_0 and B_1 inhomogeneities, asymmetry of the B_1 transmit/receive fields, eddy currents, and relaxation processes—all constituting additional factors that might bias a genuine assessment of the imaging properties in question. A straightforward one-dimensional (1D) gradient-echo sequence was chosen as the basis for these comparisons. This choice was deemed sufficient in the present context, as all current SPEN implementations involve the incorporation of spatiotemporal-encoding solely along one axis (either RO, PE, or SS) of a multidimensional imaging pulse-sequence. Further considerations regarding the generalization of this analysis to implementations of SPEN along more than one dimension are given in the Discussion.

Simulations were programmed in C++ and MATLAB (The MathWorks Inc., Natick, MA), and were based on full time and space propagation of spins according to Bloch equations. Image reconstruction was subsequently performed using Fourier Transform for k-space encoded signals, and SR reconstruction for SPEN data. The latter was based on solving the LSM problem in Eq. [5] using a single nonregularized iteration as described in Ben-Eliezer et al (26). Zero-padding of the k-space encoded data was done before calculating its corresponding PSF. A similar interpolation procedure was repeated for the SPEN data, implemented in this case by using a high resolution version of the reconstruction model, designed so as to produce the same number of pixels as the zero-padded FT data set. All SPEN and k-space encoded simulations, as well as the postprocessing codes are available upon request.

Images' SNR were evaluated using a Monte-Carlo approach, where multiple runs of the same imaging sequence were repeatedly simulated ($N^{sim}_{repetitions} = 256$) – each time with a different noise vector. The noise for each run was generated using MATLAB's random seed generator, and synthesized to have a zero-mean Gaussian distribution, and standard-deviation equal to ~1% of the maximal magnetization intensity. Image domain SNR maps were then evaluated by taking the N-point time-series of each image pixel and dividing their mean by their standard-deviation:

$$SNR(x) = \frac{mean\left\{\hat{S}_i(x)\right\}}{STD\left\{\hat{S}_i(x)\right\}} \quad i = 1,2,\ldots,N_{repetitions} \quad [19]$$

As a final step, we compared SNR results of SR SPEN versus Fourier-based k-space encoding by calculating the ratio (SPEN SNR)/(k-space SNR) for each image pixel after their corresponding processing, and evaluated this value against the theoretical prediction given in Eq. [18].

High-Resolution Phantom Experiments

To further validate the theoretical and simulated findings, experimental SNR measurements were performed using the SPEN and k-space encoded protocols shown in Figure 2. Data were acquired on a 7T whole body Siemens scanner (Siemens Healthcare, Erlangen, Germany) using a standard dual channel birdcage head coil. Experiments involved acquiring $N^{exp}_{repetitions} = 70$ replicates of a single axial slice of a high-resolution water phantom. This procedure was repeated twice, once for each encoding

scheme, resulting in two time-series data sets. The choice of a high-resolution phantom allowed to verify that similar spatial resolutions are delivered by the two encoding schemes—a factor which would otherwise directly affect the images' intensity and bias the SNR comparison. Common imaging parameters included: repetition time (TR) = 600 ms, echo time (TE) = 9.0 ms, excitation flip-angle = 20°, refocusing flip-angle = 180°, field of view (FOV) = 128 × 128 mm^2, matrix-size=128 × 128, slice-thickness=1 mm, bandwidth = 401 Hz/Px, and SAR = 11% for SPEN-SE and 8% for the k-space encode SE protocol. SPEN frequency sweep excitation was implemented by a time modulation of the RF transmitter-phase, leading to a sweep rate of R = 20.6 kHz/ms for a duration of T_{exc} = 2500 us and over a range of BW_{exc} = 51.4 kHz, designed to match the acquisition bandwidth BW_{acq}. Experimental data were processed in MATLAB using SR reconstruction for the SPEN-based scheme in Figure 2a, and using conventional FT for the k-space encoded protocol in Figure 2b. Two-dimensional SNR maps were subsequently calculated by taking the 70-point time-series at each image location, removing the first 6 data points to avoid any pre steady-state effects, applying a linear baseline correction procedure according to (32) (order = 1, cost-function = "stq", threshold = 0.0385), and calculating the resultant SNR according to Eq. [19].

RESULTS

Numerical Calculations

Figure 4 provides graphical representations of SPEN and k-space encoded PSFs: Figure 4a displays single-source-point PSFs, while Figures 4b–4c exemplify SR-SPEN and FT k-space functions for two adjacent source points. Simulations were noise free and used the exact same imaging parameters. Almost identical PSFs and image profiles are seen for the two encoding methods, suggesting that apart from negligible differences in the contribution of distant side-lobes, similar spatial-resolutions can be realized using either method. It should be noted SPEN's PSF structure, agrees well with previous quadratic phase reconstruction results presented in (6). Considering, furthermore, the comparability to the FT based PSF suggests that both the reconstruction process in Eq. [5], as well as the one in Eq. [6], are able to effectively deconvolve the quadratic phase profiles and provide optimal image domain PSFs.

A first assessment of SPEN's SNR was obtained by means of numerical calculations of the $\left[\Sigma \mathbf{P}^{*}_{p,i}\mathbf{P}_{i,p}\right]^{1/2}$ term in Eq. [16], signifying the noise enhancement associated with the super resolution reconstruction scheme. Numerical calculations using various sets of parameters showed this noise matrix to have nearly constant diagonal values equal to $\sqrt{N}$, similar to the eigenvalues of an FT operator. Small deviation from this value did show up as slightly lower noise levels at the FOV edges. These were nonetheless balanced by a similar decrease in the calculated signal level. In accordance to Eq. [18], this result predicts that super-resolved SPEN and k-encoded FT imaging will have similar SNR values.

Figure 5 presents further validation of this hypothesis, showing the results of 1D gradient-echo simulations

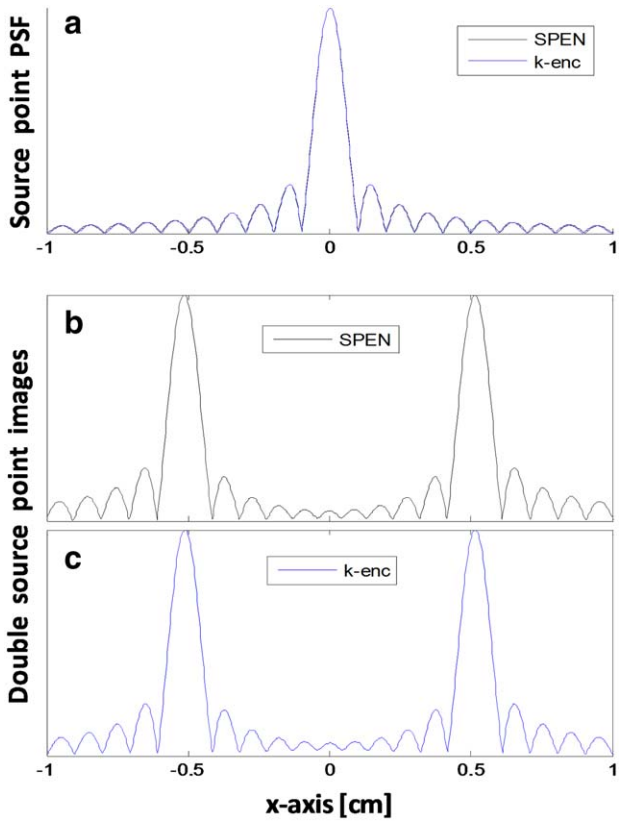

FIG. 4. Full Bloch simulation-based comparison of SPEN and k-space encoding. **a:** Simulated image-domain PSFs exhibiting an almost identical spatial profiles. **b,c:** Two source points (b) SPEN and (c) k-space encoded simulated MR image. A slight difference is seen at the center of the imaged FOV, corresponding to the PSF edges, and resulting from edge effects in SPEN's super-resolved processing. [Color figure can be viewed in the online issue, which is available at wileyonlinelibrary.com.]

comparing the performance of SR SPEN and of k-space FT MRI, in the presence of noise. Similar image quality is produced by both encoding schemes (Fig. 5a), revealing the underlying object profile perturbed by the noise that was added to raw signal before reconstruction. Figures 5b and 5c portray SNR maps calculated based on Eq. [19] for the two encoding schemes, and the corresponding ratio between these values. Equal SNR levels clearly characterize both encoding methods, whilst exhibiting no apparent spatial dependency. Similar results were also obtained when setting the initial magnetization to zero and executing noise-only simulations (not shown). These computer-based findings were in close agreement with the analytical calculations, and further corroborate the hypothesis that SR SPEN and k-space encoded MRI have comparable SNR levels.

Experimental SNR Estimations

Figures 6 and 7 summarize the experimental SNR estimations performed using the pair of SPEN and k-space encoded sequences shown in Figure 2, for a high-resolution phantom. In these images the vertical (RO) axis was either spatiotemporally or k-space encoded, whereas the other two axes used phase-encoding along the horizontal (PE) axis, and slice-selection along the

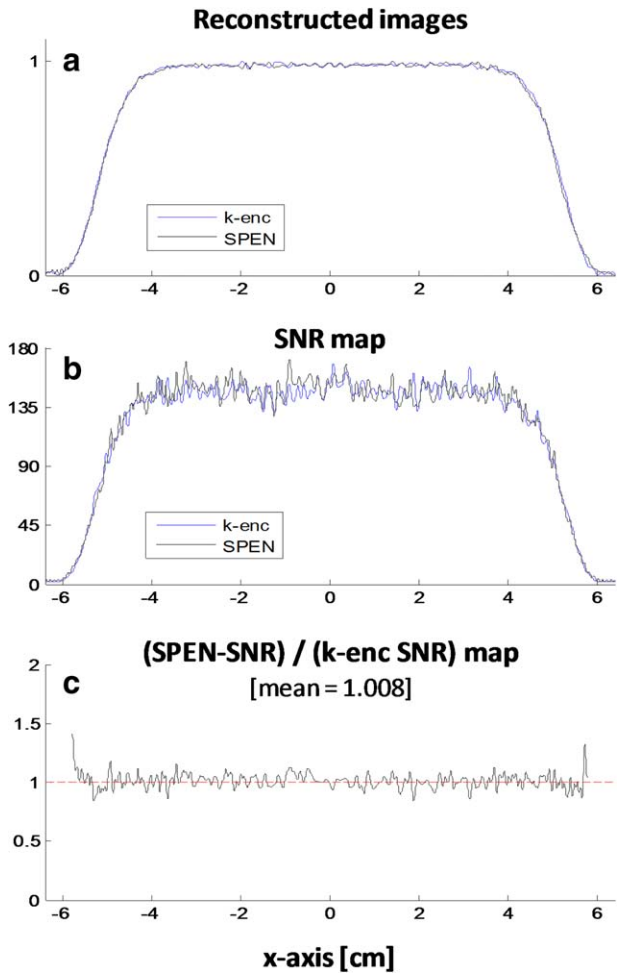

FIG. 5. Simulation based comparison of the relative SNR values for SPEN and for k-space encoded MRI. **a:** Representative images resulting from SPEN and k-space encoding for a smoothly varying 1D object with a constant magnetization amplitude along its central region. Random, zero mean, white Gaussian noise was incorporated into the simulated signal and is expressed as small variations in the reconstructed images. **b:** SNR map produced by repeating the simulations for $N_{repetition} = 256$ times (each time using a difference noise vector), followed by calculating the ratio between the mean and the standard-deviation of the signal time-series at every image pixel. **c:** Ratio of the SPEN-SNR / k-space SNR, exhibiting a mean value of unity. [Color figure can be viewed in the online issue, which is available at wileyonlinelibrary.com.]

through-plane (SS) axis. Images were acquired for the axial slice shown in Figure 6a, chosen so as to include both uniform and high-resolution features. Figures 6b–6f present zoomed images of the 16×16 mm^2 ROI marked by the dashed inset in Figure 6a, acquired using a reference high resolution FLASH imaging protocol, and the SPEN and k-space spin-echo sequences in Figure 2. Figures 6d–6f hold SPEN based images, which were all reconstructed from the same data set using either full SR reconstruction (6d); SR reconstruction modified by setting uniform spatial weights $W_{u,n} = 1$ in Eq. [7] (6e); and using Fourier Transform (6f). As was demonstrated in Figure 3 above, all three postprocessing options will deliver images of similar quality as long as the underlying data set was sampled under the Nyquist criteria. Despite the similar experimental and shimming conditions small differences emerge, however, at close examination of the SR SPEN and k-space encoded images at Figures 6c and 6d. These mainly include different distribution of Gibbs ringing artifact, and slight blurring of the k-space encoded features versus the SPEN-based image. We ascribe the latter different to T_2* relaxation effects which, even in an ideal spin-echo sequence, will still influence the peripheral parts of the k-space and thus distort the high-resolution features of the image. SPEN based sequences, on the other hand, offer more robust spin-echoes (12) where each part of the signal undergoes its own T_2* refocusing, allowing more reliable mapping of the object's high-resolution features. These factors aside, the images in Figures 6b and 6c display very similar spatial resolutions in agreement with the similarity between the PSFs of these two encoding schemes.

Experimental 2D SNR maps were produced from these data using Eq. [19], by evaluating the ratio between the mean and the standard-deviation of each image pixel over a series of 64 consecutive images. Figures 7b–7e contain four representative SNR profiles taken along the RO dimension at the positions indicated in Figure 7a, from SR SPEN and k-encoded data sets. Quantitative SNR values are given above each plot, representing the mean ratio between SPEN and k-space encoded data along each profile, and estimated for regions where the image intensity was above 25% of its maximal value. Almost identical values were obtained for both encoding methods, once again confirming their SNR equivalence.

DISCUSSION

The formalism and results presented in this report lay a general framework for the implementation of SPEN imaging and for the evaluation of its corresponding resolution and sensitivity characteristics. It is shown that by predicating the target image parameters, namely, the field-of-view, spatial-resolution and acquisition bandwidth, this framework allows one to derive all experimental and reconstruction parameters required for SPEN, leading to a minimal width image-domain PSF. Theoretically, this framework predicts that equal spatial-resolution and SNR can be reached for SR SPEN as compared to conventional k-space encoded FT MRI. This prediction was substantiated using analytical calculations, simulations, and experimentally using gold-standard SNR measurements. The experimental approach taken in this study relied on phantom rather than in vivo imaging, as the latter is more error prone when evaluating SNR due to its inability to acquire a series of images under perfectly identical settings, and in addition, due to its dependence on the regions chosen for representing the signal and the noise, and its high sensitivity to motion artifacts. We, therefore, deem the phantom-based approach adopted in this work as the most faithful way of assessing SPEN's SNR comparativeness, and anticipate our finding's principal aspects to persist for in vivo applications.

The numerical and experimental estimations of SR SPEN SNR relied on the specific reconstruction model in Eq. [6]. This noniterative LSM model hereby used has

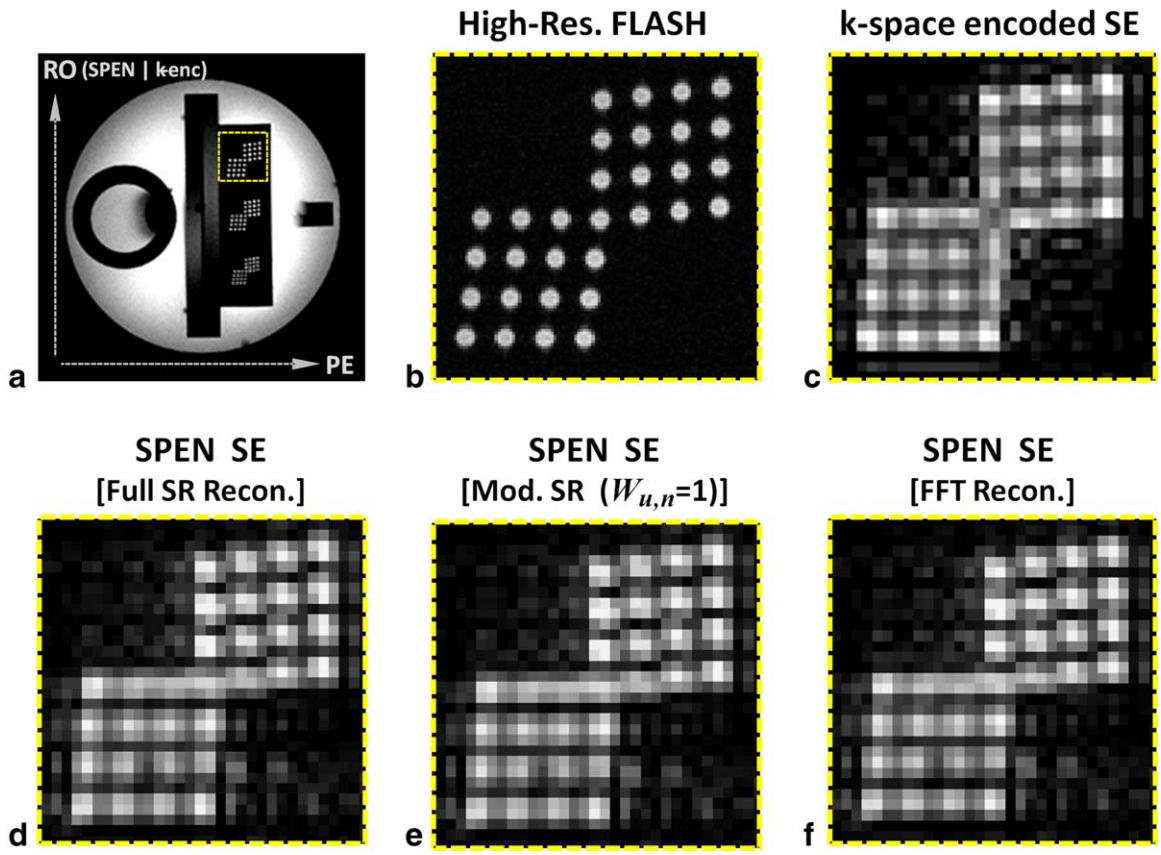

FIG. 6. Representative images of the high-resolution phantom used in this study. **a:** Full FOV image of the phantom. Experiments used either SPEN or conventional k-space encoding along the RO (vertical) axis and similar phase-encoding along the PE (horizontal) axis. b–f: Zoomed images of a 16 $\times$ 16 mm^2 region of interest (ROI) marked by a yellow dashed inset in (a). **b:** Reference high-resolution FLASH image. **c:** k-space encoded Spin-Echo image. **d–f:** SPEN based Spin-Echo images reconstructed from the same data set using full SR reconstruction (d); SR reconstruction modified to use uniform spatial weights $W_{u,n}=1$ in Eq. [7] (e); and Fourier Transform (f). All three SPEN postprocessing options deliver images of similar quality, in agreement with the results shown in Figure 3 for data sets whose sampling rate meets the Nyquist criteria. Some differences, however, can be seen between the k-space encoded and SPEN images in (c) and (d), (e.g., the different Gibbs ringing distribution) reflecting the differences between the two encoding methods that were at play in each case. Notwithstanding these differences, roughly similar spatial-resolutions can be realized by both methods when following SPEN's parametric regime and SR reconstruction procedure described in the text. [Color figure can be viewed in the online issue, which is available at wileyonlinelibrary.com.]

been previously shown to provide robust and reliable reconstructions under various in vivo settings (15,22,29,30); in the present context, it provided Fourier-equivalent SNR levels whilst exhibiting no loss in spatial-resolution. Other SPEN postprocessing models have also been recently proposed (21,33). To the best of

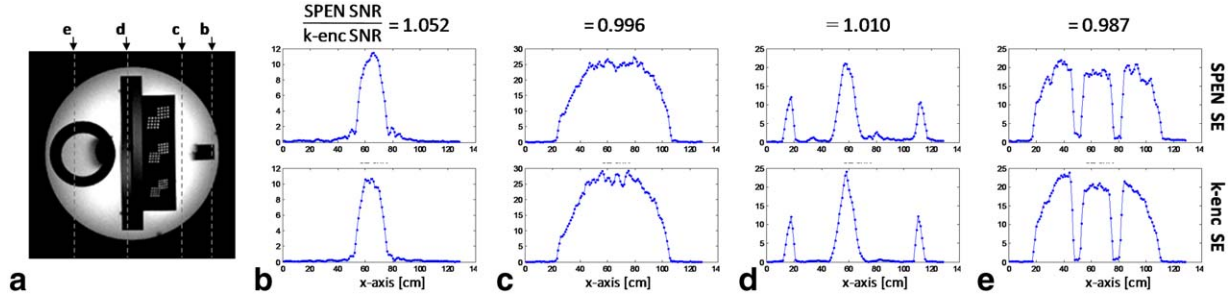

FIG. 7. Experimental SNR comparison between SPEN and k-space encoding for the high resolution phantom in (**a**), using identical imaging parameters. **b–e:** SNR values for 1D profiles, taken along the SPEN | k-encoded (vertical) axis at four representative x-locations marked by the gray dashed lines in (a). Quantitative numerical value denotes the mean ratio between the corresponding SNR values. To avoid noise-only regions, estimation included regions where the signal level was more than 15% of its maximal intensity. Similar (SPEN-SNR) / (k-enc SNR) values are seen for all x-locations of the object, revealing quantitatively similar SNR levels for both methods. The full set of imaging parameters is delineated in the Methods section. [Color figure can be viewed in the online issue, which is available at wileyonlinelibrary.com.]

our understanding, these do not differ inherently from the model used herein, and should therefore offer comparable SNR and spatial resolution. The ability to bring SPEN's SNR up to par with SNR values of FT-based imaging is indeed embodied in all above models. It derives from the initial use of a wide focal point, combined with the localized nature of the reconstruction operator **P** which, as previously indicated in (24), restricts the dynamic range used during reconstruction, resulting in decreased noise levels. Equally important is the convex nature of the SR problem which makes it well behaved numerically, and hence enables an efficient multiplexing of multiple signal points during reconstruction.

It is important to note that, although the specific parameter values used in this study were derived from the ones used in conventional k-space imaging (thereby allowing objective comparison of the two encoding methods) SPEN is not necessarily restricted to this parametric limit, which is essentially defined by the Nyquist criterion (11). The SNR comparability of SPEN and Fourier encoding in this limit thus does not exhaust the capabilities of SPEN, e.g., its capacity for inherent spatial localization or its enhanced robustness against off-resonance artifacts. These capabilities can still be used while keeping in mind the SNR tradeoff defined by Eqs. [12] and [16] that will arise when shifting from the spatially global k-space limit toward higher spatial localization.

SPEN's higher efficiency in refocusing off-resonance frequency shifts such as static field inhomogeneities and chemical-shift distortions can become a significant aid in single-shot imaging, when substituting the artifact-prone phase-encoded (PE) dimension with spatiotemporal-encoding. Because SPEN is only required to match the acquisition and excitation time-bandwidth products, higher freedom is available for increasing the acquisition bandwidth along this 2nd dimension while avoiding Nyquist ghosting artifacts owing to SPEN's spatially local nature (11,12). Furthermore, as SPEN is in such instances still implemented only along a single (PE) dimension, the SNR characteristics of these implementations will follow along the lines delineated in this report. From the relations in the Theory Section it can be inferred that SR SPEN will then lead to similar PSF profiles as an ideal phase-encoding and entail no SNR losses—while continuing to offer enhanced T_2* refocusing capabilities. An intriguing option that arises in these "Hybrid" SPEN-/k-encoded 2D single-shot experiments is the new degree of freedom in trading off SNR for higher bandwidths along the SPEN dimension. Increasing the time-bandwidth product (TBP) of SPEN's matched encoding / decoding processes (Eq. [10]) will then offer higher immunity against frequency off-resonance effects manifested as reduced distortion of the spatiotemporally encoded axis $x^{distorted} = x + \Delta B_0/G_{acq}$, and lower signal attenuation embodied in the Jacobian of the transformation between the original and distorted coordinate systems (see Supp. Materials, which are available online, for a full analysis of these effects). It is important to note that although this is a very effective tool for animal studies, clinical scanners will impose certain limitations on the allowed TBP. Quantitatively, this value correlates linearly with either higher SAR levels or longer excitation / acquisition durations, and might, therefore, limit short-TE or SAR demanding applications (12). Pertaining to SNR, an increased TBP will lead to a thinner focal region and attenuation of the acquired signal according to Eq. [10], indicating that an F-fold increase in the excitation / acquisition TBP will decrease the image intensity $\hat{S}^{SPEN}$ by the same factor. The reconstructed image noise STD will, however, also subsequently decrease, as the higher TBP along the SPEN dimension will lead to increased spatial localization of the reconstruction matrix **P** in Eq. [16], and to a $\sqrt{F}$ lower noise amplification. The time-domain noise $\chi^{(k)}$ will, at the same time, remain unchanged, owing to the fact that in single-shot imaging the acquisition bandwidth is dictated by the much larger readout gradient. Factoring these two effects together, an overall SNR penalty of only $\sqrt{F}$ will need to be traded off for an F-fold increase in the protocol's bandwidth along the PE dimension, allowing higher immunity to off-resonance artifacts (see Supp. Materials for additional analysis of these effects). As single-shot protocols use high excitation flip-angles they are typically rich in SNR, making this tradeoff a powerful and indeed "cost-effective" tool for reducing field-inhomogeneity, motion, and chemical-shift artifacts. SPEN-based single-shot protocols can thus use longer echo times, realize larger matrix sizes, and be used to scan regions which were so far inaccessible to single-shot imaging (14).

Frequency-swept pulses serve as the basis of SPEN-based imaging and spectroscopy applications, and give rise to new and unique capabilities pertaining to both these fields. Their use in MRI, however, has two restrictive aspects that should be carefully considered. The first of these restrictions relates to the high bandwidths of these pulses and the ensuing increase in SAR values. Similar to its positive effect on the signal-to-noise ratio, the SR reconstruction has a vital role also in this case: by removing the stringent constraint of encoding a one-pixel-wide PSF, lower B_1 powers can be used without loss of spatial-resolution, enabling lower SAR deposition (26). Evaluation of the concrete SAR penalty vis-à-vis standard slice-selective pulses remains a question of the specific application at hand and, in the end, will depend on the balance between SPEN FOV and slice thickness, as well as on the slice-selection scheme and the B_0 field strength. Another limiting feature drawing from the spatially sequential excitation and acquisition processes, is a spatially dependent echo-time (TE) and subsequently T_2 weighting of the sample. Although this does not constitute a major complication when implementing SPEN along the fast RO dimension, it can become significant in single-shot applications involving long echo times. Solutions for this issue have been suggested (11,12), while other alternatives to deal with this effect are currently being explored.

Extended implementations using SPEN along more than a single dimension in combination with super-resolution processing, are possible and might hold their own merits. Generalization of the presented analysis to higher dimension will in these cases depend mainly on the correlation between the different SPEN dimensions. Assuming for example, a straightforward implementation of SPEN along two independent axes of a rectilinear Cartesian grid, both the spatial-resolution and SNR findings

in this report would maintain their validity, separately for each of the dimensions. Analysis of more complex multidimensional trajectories, such as a spiral imaging, would require formulating the interrelation between the encoded axes (both during the encoding, and during the acquisition) and would be specific to the particular implementation at hand. Further consideration should also be given to the generalization of the presented analysis to multi-coil receive systems. This would, as a first step, require the noise STD in Eq. [14] to include the full coil correlation matrix Ψ, leading to a spatial variation of the SNR according to the coil sensitivity profiles. This being said, it is likely that such setups would in fact favor a SPEN-based approach, owing to this method's ability to localize the signal in each coil to its spatially optimal region, and exclude low sensitivity regions which offer mainly noise contributions.

APPENDIX A

Derivation of SPEN's SR Factor F_{SR} Under Optimal Reconstruction Conditions

The super-resolution factor in SPEN reconstruction is defined as the ratio between the encoded pixel size Δx, and the reconstructed pixel size dx. It is important to remember that, while Δx is determined experimentally according to the curvature of the excitation quadratic phase profile in Eq. [1], the value of dx is a parameter of the reconstruction and can be arbitrarily set. The choice is, however, trivial as one would most likely aim for the highest possible nominal resolution $dx = FOV / N$, where FOV is the imaged field-of-view and N the number of acquisition points. Using Eq. [2] the super-resolution factor can be expressed as,

$$F_{SR} = \frac{\Delta x}{dx} = \frac{\sqrt{R}/\gamma G_{exc}}{FOV/N} \qquad [A.1]$$

where R denotes the sweep rate of the encoding RF pulse [in units of (Hz/s)]. Expressing the value of R explicitly using the excitation bandwidth $\gamma G_{exc} FOV$ and duration T_{exc}, while remembering SPEN's prerequisite for equal time $\times$ bandwidth values during the excitation and the acquisition (see Eqs. [12] and [13] in Ref. (10)) we get,

$$F_{SR} = \frac{\sqrt{\gamma G_{exc} FOV / T_{exc}}}{\gamma G_{exc}} \frac{N}{FOV} = \frac{N}{\sqrt{\gamma G_{acq} FOV}\sqrt{T_{acq}}} = \frac{N}{\sqrt{\gamma G_{acq} FOV}\sqrt{T_{acq}}} \qquad [A.2]$$

Setting the acquisition dwell time dt to be one over the acquisition bandwidth $\gamma G_{acq} FOV$ yields the required relation,

$$F_{SR} = \frac{N}{\sqrt{T_{acq}/dt}} = \sqrt{N} \therefore \qquad [A.3]$$

ACKNOWLEDGMENTS

The authors thank Dr. Kai Tobias Block for fruitful discussions, Leeor Alon for helping with the experiments, and Dr. Christian Geppert for inspiration. This research was supported by the Kamin-Yeda Project 711237 (Israel Ministry of Trade and Industry), ERC Advanced Grant #246754, The Helen and Martin Kimmel Award for Innovative Investigation, and the generosity of the Perlman Family Foundation.

REFERENCES

1. Lauterbur PC. Image formation by induced local interactions: examples employing nuclear magnetic resonance. Nature 1973;242:190–191.
2. Shrot Y, Frydman L. Spatially encoded NMR and the acquisition of 2D magnetic resonance images within a single scan. J Magn Reson 2005;172:179–190.
3. Kunz D. Use of frequency-modulated radiofrequency pulses in MR imaging experiments. Magn Reson Med 1986;3:377–384.
4. Johnson G, Wu EX, Hilal SK. Optimized phase scrambling for RF phase encoding. J Magn Reson Series B 1994;103:59–63.
5. Maudsley AA. Dynamic range improvement in NMR Imaging using phase scrambling. J Magn Reson 1988;76:287–305.
6. Pipe JG. Spatial encoding and reconstruction in MRI with quadratic phase profiles. Magn Reson Med 1995;33:24–33.
7. Parker DL, Hadley JR. Multiple-region gradient arrays for extended field of view, increased performance, and reduced nerve stimulation in magnetic resonance imaging. Magn Reson Med 2006;56:1251–1260.
8. Hennig J, Welz AM, Schultz G, Korvink J, Liu Z, Speck O, Zaitsev M. Parallel imaging in non-bijective, curvilinear magnetic field gradients: a concept study. MAGMA 2008;21:5–14.
9. Stockmann JP, Ciris PA, Galiana G, Tam L, Constable RT. O-space imaging: highly efficient parallel imaging using second-order nonlinear fields as encoding gradients with no phase encoding. Magn Reson Med 2010;64:447–456.
10. Tal A, Frydman L. Spatial encoding and the acquisition of high definition MR images in inhomogeneous magnetic fields. J Magn Reson 2006;181:179–194.
11. Chamberlain R, Park JY, Corum C, Yacoub E, Ugurbil K, Jack CRJ, Garwood M. RASER: a new ultrafast magnetic resonance imaging method. Magn Reson Med 2007;58:794–799.
12. Ben-Eliezer N, Shrot Y, Frydman L. High-definition single-scan 2D MRI in inhomogeneous fields using spatial encoding methods. Magn Reson Imaging 2010;28:77–86.
13. Airaksinen AM, Niskanen JP, Huttunen JK, Nissinen J, Garwood M, Pitkanen A, Grohn O. Simultaneous fMRI and local field potential measurements during epileptic seizures in medetomidine-sedated rats using raser pulse sequence. Magn Reson Med 2010;64:1191–1199.
14. Goerke U, Garwood M, Ugurbil K. Functional magnetic resonance imaging using RASER. Neuroimage 2011;51:350–360.
15. Ben-Eliezer N, Solomon E, Harel L, Nevo N, Frydman L. Fully refocused multi-shot spatiotemporally encoded MRI: robust imaging in the presence of metallic implants. MAGMA 2012;25:433–442.
16. Schmidt R, Frydman L. New spatiotemporal approaches for fully refocused, multislice ultrafast 2D MRI. Magn Reson Med 2014;71: 711–722.
17. Ben-Eliezer N, Frydman L, Sodickon DK. Comprehensive theoretical and experimental analysis of the parametric framework and SNR of super-resolved spatiotemporally-encoded (SPEN) MRI. In Proceedings of the 21st Annual Meeting of ISMRM, Salt Lake City, Utah, 2013. p. 2681.
18. Tal A, Frydman L. Spectroscopic imaging from spatially-encoded single-scan multidimensional MRI data. J Magn Reson 2007;189:46–58.
19. Schmidt R, Frydman L. In vivo 3D spatial/1D spectral imaging by spatiotemporal encoding: a new single-shot experimental and processing approach. Magn Reson Med 2013;70:382–391.
20. Ito S, Yamada Y. Alias-free image reconstruction using Fresnel transform in the phase-scrambling Fourier imaging technique. Magn Reson Med 2008;60:422–430.
21. Chen Y, Li J, Qu X, Chen L, Cai C, Cai S, Zhong J, Chen Z. Partial Fourier transform reconstruction for single-shot MRI with linear frequency-swept excitation. Magn Reson Med 2013;69:1326–1336.
22. Ben-Eliezer N, Frydman L. Spatiotemporal encoding as a robust basis for fast 3D In Vivo MRI. NMR Biomed 2011;24:1191–1201.
23. Meyerand ME, Wong EC. A Time encoding method for single-shot imaging. Magn Reson Med 1995;34:618–622.
24. Pipe JG. Analysis of localized quadratic encoding and reconstruction. Magn Reson Med 1996;36:137–146.

25. Tal A, Frydman L. Single-scan multidimensional magnetic resonance. Prog Nucl Magn Reson Spectrosc 2010;57:241–292.
26. Ben-Eliezer N, Irani M, Frydman L. Super-resolved spatially-encoded single-scan 2D MRI. Magn Reson Med 2010;63:1594–1600.
27. Pruessmann KP, Weiger M, Scheidegger MB, Boesiger P. SENSE: sensitivity Encoding for Fast MRI. Magn Reson Med 1999;42:952–962.
28. Sodickson D, McKenzie C. A generalized approach to parallel magnetic resonance imaging. Med Phys 2001;28:1629–1643.
29. Solomon E, Pyatigorskaya N, Bendel P, Le Bihan D, Ciobanu L, Frydman L. The origins of fMRI contrast in SPEN imaging at ultra high magnetic fields. In Proceedings of the 20th Annual Meeting of ISMRM, Melbourne, Australia, 2012. p. 2070.
30. Ben-Eliezer N, Goerke U, Ugurbil K, Frydman L. Functional MRI using super-resolved spatiotemporal encoding. Magn Reson Imaging 2012;30:1401–1408.
31. McCllelan J, Parks T. Eigenvalue and eigenvector decomposition of the discrete Fourier transform. IEEE Trans Audio Electroacoustics 1972;20:66–74.
32. Mazet V, Carteret C, Brie D, Idier J, Humbert B. Background removal from spectra by designing and minimising a non-quadratic cost function. Chemom Intell Lab Syst 2005;76:121–133.
33. Shen J, Ziang Y. High fidelity magnetic resonance imaging by frequency sweep encoding and Fourier decoding. J Magn Reson 2010; 204:200–207.